Digital Image-based Elasto-Tomography: First experiments in surface based mechanical property estimation of gelatine phantoms

Ashton Peters[1], Stefan Wortmann, Rodney Elliott, Mark Staiger,
J. Geoffrey Chase, Elijah Van Houten

Keywords: Computational Mechanics, Elasticity, Finite Element Method,
Inverse Problem.

[1]Department of Mechanical Engineering, University of Canterbury, Private Bag 4800, Christchurch, New Zealand, ape20@student.canterbury.ac.nz

Abstract

Digital Image-based Elasto-Tomography (DIET) is a novel surface-based elasticity reconstruction method for determining the elastic property distribution within the breast. Following on from proof of concept simulation studies, this research considers the motion evaluation and stiffness reconstruction of a soft tissue approximating gelatine phantom. This initial phantom work provides an intermediate stage between prior simulation studies more detailed phantom studies to follow. Reference points on the surface of a cylindrical phantom were successfully tracked and converted into a steady-state motion description. Motion error based mechanical property reconstruction allowed an estimation of the stiffness of the gelatine when actuated at 50 Hz. The reconstructed stiffness compared favorably with independently measured stiffness properties of the gelatine material when experimental assumptions were considered. An experimental noise estimate of 50% was confirmed accurate by comparing experimental motions to simulated motion data with added noise.

1 Introduction

Manual palpation performed by self-examination or physician is the most common method for detecting abnormal lesions within the breast. The ability to detect anomalies using this method is a result of the underlying mechanical properties of the tissue. More specifically, a consequence of the cellular structure and density of cancerous tissue is that it is stiffer than surrounding healthy breast tissue. Experimental measurements of the elastic properties of healthy and cancerous breast tissue have confirmed that invasive ductal carcinoma are up to an order of magnitude stiffer than the surrounding fibroglandular tissue [1, 2]. Several other groups have successfully reconstructed the mechanical properties of breast tissue using Magnetic Resonance (MR) elastography and ultrasound elastography, with calculated modulus values comparable to those from direct mechanical measurement [3–5].

Elastographic techniques for breast imaging are based on the inherent tissue stiffness contrast of cancerous tissue. This contrast is far greater than the x-ray attenuation contrast measured with a screen-film mammogram, regarded as the gold standard for breast cancer screening [6]. Several groups have had success in reconstructing the elastic properties of the breast volume using different elastographic methods. MR-based modalities measure induced breast motion by means of phase-contrast gradient methods. Carefully controlled imaging techniques and processing of the data sets allows three dimensional motion data throughout the breast volume to be obtained at voxel resolution. Inverse problem mechanical reconstruction algorithms based on full motion data sets have been used to convert this motion information into a tissue stiffness distribution [4]. Ultrasound elastography determines tissue stiffness estimates from measurements of propagating sound waves within tissue [7–9]. While this approach is significantly less expensive than MR based methods, it suffers from a lack of image contrast and limited off-axis resolution. Research in both MR and ultrasound elastography is ongoing.

Digital Image-based Elasto-Tomography (DIET) is a novel method currently under development in the field of soft tissue elastography. The DIET system uses only surface tissue motion as the inverse reconstruction input to an algorithm that calculates the internal stiffness distribution of the sample being examined. This reconstruction problem has less data and therefore greater computational intensity than full volume problems. However, the

ability to obtain the reconstruction solution without the need for expensive and/or invasive methods such as MRI make the approach practically and clinically attractive.

Physiological aspects and the physical location of the female breast make it an ideal candidate for a novel, non-invasive, surface motion based property reconstruction technique such as DIET. An outline of the major steps in the DIET process follows:

1. A steady-state sinusoidal motion is induced throughout the breast volume by an actuator placed against the surface of the breast.

2. Spatially calibrated digital imaging sensors arrayed around the breast capture sequential two-dimensional images of reference points on the surface of the breast as they cycle through the full range of steady-state motion.

3. Image processing algorithms and estimation techniques convert consecutive sets of two-dimensional images of each reference point on the breast surface into a three-dimensional motion vector map, with magnitude and phase.

4. The three-dimensional amplitude of each reference point's motion is used in an inverse reconstruction algorithm that generates an elastic modulus distribution within the three-dimensional breast volume.

Proof of concept studies for the DIET system, including a detailed discussion of the camera calibration system and digital imaging motion sensing, the inversion algorithm, and basic simulation studies, are outlined in more detail in [10]. The research presented here reports on the first experiments evaluating the techniques required to successfully image the surface of soft tissue emulating phantoms and to estimate their stiffness - a first experimental proof of concept evaluation. Single-phase phantoms will provide a natural progression between prior simulation studies and a future multi-phase phantom studies that provides a closer match to the expected clinical scenario. They also provide a known solution that is readily validated, as in this study, by mechanical property testing.

In the envisaged final clinical application of the DIET system, stiffness resolution will need to be such that healthy tissue can be easily differentiated from potentially unhealthy tissue. The final system will require the ability to

resolve tissue stiffness to within an accuracy of approximately ±10kPa. This resolution should clearly be able to differentiate significantly stiffer unhealthy tissue.

2 Methods

A necessary pre-requisite of testing the DIET system *in vivo* is an evaluation phase using phantoms designed to closely approximate the behavior of soft tissue. Testing computational and processing algorithms, and system hardware on phantoms of known mechanical properties should allow evaluation and refinement of the system under a controlled environment. In this experiment, gelatine phantoms that approximate soft tissue were used to test the procedure for obtaining surface motion from an actuated sample. In addition, the mechanical properties of the phantom material were tested by independent techniques, providing benchmark measurements against which mechanical property estimation methods could be evaluated.

2.1 Phantom Preparation

A gelatine-based hydrogel was used in this study because of its linear elastic behavior and similar mechanical properties to human soft tissue [11]. Variation in the composition of the gelatine allowed control over the resulting Young's modulus of the phantom. The composition of the phantom tested in this study is listed in Table 1. A Young's modulus value of between 10 kPa and 50 kPa was desired, matching the range expected for healthy breast tissue [3]. Preparation of the gelatine phantom involved the following steps:

1. Hot water at approximately 70 °C was mixed with 2-Propanol, used to alter the sound speed in the finished phantom. While this mixture was not imperative in this case, as the testing did not involve ultrasound, the addition ensured the compression wave speed was similar to that of soft tissue.

2. Powdered gelatine (20A grade) was added slowly and dissolved. Mixing continued for approximately 15 minutes.

3. When the temperature of the mixture had decreased to approximately 40 °C, Formaldehyde was added to start the cross-linking process.

4. The final mixture was poured into a cylindrical mold of diameter 70mm up to a height of 50mm and left for 24 hours to congeal at room temperature.

2.2 Mechanical Testing

Mechanical testing samples were taken from a concurrently produced gelatine batch for mechanical property measurements. These samples were tested at room temperature 24 hours after preparation. Long cylindrical samples were taken from a larger block using a sharp hollow cylindrical cutter approximately 10 mm diameter. The cylinder was then cut into 3–5 mm lengths with parallel ends using a razor blade to produce compression samples. This method ensured that the samples came from the interior of the phantom, and had not hardened as a result of exposure to the air.

The mechanical property testing of the gelatine was carried out using a Dynamic Mechanical Analyzer (Diamond DMA, Perkin Elmer Instruments Inc). Static compression testing was performed to a strain approaching 10%, which is the upper limit of the gelatine's linear-elastic range [11]. Multiple samples were tested to obtain an average result for comparison to the phantom.

Dynamic testing was carried out on the DMA to determine viscoelastic properties. However, the samples' elasticity was just below the range that could be tested accurately by the machine. This, in the present work the material testing was limited to the static case. Errors introduced by this limitation are discussed later in this article.

2.3 Displacement Imaging

A test apparatus was developed to image the surface motion of the gelatine phantom model, as shown in Figure 1. The phantom was placed on a horizontal plate and driven to steady-state harmonic motion by a linear voice coil actuator (VP5M, Derritron Electronics Ltd) coupled to a 300 W amplifier (DCP3, Derritron). Applied actuation was 1.2 mm peak-to-peak at 50 Hz. Two commercially available digital cameras (Olympus C-4040 Zoom and Canon PowerShot G6) were used for image acquisition, and connected to an image processing computer. Both cameras were focused on the center of the actuation plate at a distance of approximately 200 mm and separated by an angle of roughly 75 degrees. Accurate positioning of the cameras was not

required because all position-dependent camera parameters are determined during the camera calibration process, as discussed in [10].

Uniform light was supplied to the scene using four 60 W lamps. A triggerable stroboscope (Dawe Transistor Stroboflash Type 1209C) was coupled to the actuator signal to freeze phantom motion for image capture. Adjusting the timing of the stroboscope illumination relative to the sinusoidal actuation signal allowed examination of the surface motion at a range of phases during the steady-state motion cycle. More specifically, strobing allows the same point in the steady-state response to be imaged over several cycles.

Actuation plate motion was measured using a Helium-Neon laser and an interferometer (Model OFV-512, Polytec) coupled to a vibrometer controller (Model OFV-5000, Polytec GmbH). The velocity information provided was used for amplitude and frequency control of the actuation system. A dSPACE^{TM} modular hardware control system was used to run this system.

Prior to motion imaging, two columns of black dots were applied to the phantom with a permanent marker. These fourteen reference points shown in Figure 2 were motion tracked with the camera system. Simultaneous left and right images were captured at a sequence of 20 degree phase offsets throughout the motion cycle using remote computer controlled image capture software. The process was repeated until two complete cycles of motion had been captured.

2.4 Motion Estimation

The tracked reference point location data required further processing before it could be directly compared with motion data generated by simulated Finite Element (FE) solution or used in mechanical reconstruction. This task involved approximating the 3D motion of each reference point with a vector representing its steady-state displacement. This was carried out by enclosing the motion path within a 3D box with dimensions equal to the peak-to-peak amplitude of each of the three orthogonal motion components Δx, Δy and Δz. The steady-state displacement of each point was then approximated as a vector,

$$\overrightarrow{d}_i = \begin{pmatrix} \Delta x/2 \\ \Delta y/2 \\ \Delta z/2 \end{pmatrix}, \tag{1}$$

where $\overrightarrow{d}_i$ represented the steady-state displacement amplitude at the ith reference point. The sign of the three components of $\overrightarrow{d}_i$ was determined by examining the measured motion track overlaid with the vector approximation.

2.5 Finite Element Simulation

A simple attempt at estimating the elastic modulus of the phantom was made using a FE model of the phantom. The phantom's assumed homogeneity meant that only a one-parameter estimate was required, eliminating the need for a more involved gradient-descent based reconstruction method. Instead basic motion error minimization was used to estimate a single stiffness parameter, to prove the concept.

The experimentally measured displacement was evaluated against the simulated displacement by comparing displacements at the fourteen reference points. Each reference point had both a measured displacement vector, $\overrightarrow{d}_i$, and simulated displacement vector, $\overrightarrow{f}(\theta)_i$. To avoid sign inconsistencies, a squared error was used,

$$F = \sqrt{\frac{\sum_{i=1}^{N} \| \overrightarrow{d}_i - \overrightarrow{f}(\theta)_i \|^2}{3N}}, \tag{2}$$

where F represented the motion error, N the number of reference points, and θ a combination of the material parameters E (Young's modulus), ν (Poisson's Ratio) and ρ (density). For the homogeneous, isotropic case, where all material properties were assumed constant, and ν and ρ were assumed known (0.49 and 1000 kg/m^3 respectively), only Young's modulus needed to be reconstructed.

A computer model of the cylindrical phantom was created and meshed using Gambit (Version 2.2.30, Fluent Inc), and is shown in Figure 2. Key model dimensions were taken from physical measurements of the actual phantom, resulting in a height of 50 mm and a diameter of 70 mm. Though the real phantom was not perfectly cylindrical, the FE model provided a close enough fit to the geometry to allow basic motion comparisons. Surface nodes on the model were manipulated so all reference points on the phantom had a collocated node in the computer model. The FE model contained approximately 37 000 linear tetrahedral elements, with FE calculations performed on a dual-processor AMD Opteron$^{\text{TM}}$ workstation with 2 GB RAM.

The bottom face of the FE model was displacement-constrained in the horizontal x-y plane and harmonically displaced in the z direction with amplitude 0.6 mm (1.2 mm peak-to-peak) and frequency 50 Hz. All other faces had free surface boundary conditions. These constraints matched the experimental conditions. Self-weight was not included in the finite element model because the observed effect of gravity on the static gelatine phantom was negligible. Full volume displacement sets were obtained from forward FE simulation at a range of homogeneous Young's modulus values. Extracted surface motions at the reference points were then used for an error based estimation of the elastic modulus of the phantom.

3 Results

3.1 Mechanical Testing

Static testing in the DMA generated the stress-strain plot shown in Figure 3 for the gelatine phantom material. The slight hysteresis visible is typical for this type of material. Assuming linear elasticity, the Young's modulus of the material was estimated from the slope of the loading (upper) portion of the stress-strain curve as 9 kPa.

3.2 Phantom Displacement

Figure 4 shows motion of the actuated phantom viewed from one of the two cameras. One complete steady-state cycle is shown at twenty degree phase increments. The motion of the fourteen reference points clearly visible. Three additional points on the upper surface of the phantom were not used in this experiment.

The output of a motion tracking algorithm was a list of 36 known locations in 3D space for each reference point, giving position information over 720 degrees of sinusoidal phantom actuation and resulting motion. Figure 5 shows the measured motion track of four reference points with the vector approximation overlaid. The origin of each plot is located at the physical, fixed reference point location in 3D space corresponding to the particular point.

3.3 Stiffness Estimation

Forward FE simulation of the cylindrical phantom model gave surface motion sets for different assumed homogeneous stiffness values ranging from 5–20 kPa. The stiffness increment for these simulations was 100 Pa, which provided a good balance between resolution and simulation time. Simulations above the measured Young's modulus value of 9 kPa were done as the slight viscoelastic nature of the gelatine meant it would be expected to frequency harden slightly when actuated at 50 Hz. The reconstructed modulus value was therefore expected to fall in the 10–20 kPa range.

A plot of the error between the measured motion and the FE solutions between 5–20 kPa is shown in Figure 6. Peaks of high motion error on the plot correspond to resonant stiffness values in the FE model where simulated displacement was large but did not match measured motion. Because the phantom was assumed homogeneous, the modulus at minimum motion error provided an estimate of the actual phantom stiffness. For this phantom, the lowest motion error corresponded to a stiffness of 12.5 kPa. Reference point motion vectors from the 12.5 kPa FE phantom simulation are shown in Figure 5 for comparison with the experimentally measured motion.

An experimental error estimation of approximately 50% was made by a comparison of the measured and simulated (12.5 kPa) motion vectors. Random, normally-distributed noise was added to each orthogonal motion component at every reference point. The amplitude of this addition was a maximum of 50% of the average motion amplitude of all points. A second error sweep was performed assuming that this noisy simulated data was a measured motion data set for reconstruction analysis, and is also plotted in Figure 6.

Two other obvious local minima on the measured motion plot are 6.1 kPa and 9.5 kPa. Noisy simulated motion error sweeps were also performed for these values. These additional results are shown compared to the experimentally measured motion result in Figure 7.

4 Discussion

The results shown in Figure 5 illustrate that a modulus estimate of 12.5 kPa for the phantom leads to a reasonable match between measured and calculated motions at several of the reference points. While this match was quite clear at points three, six, and ten, it was poor at point five.

The motion discrepancy at point five provides evidence that reducing motion measurement error should lead to an improved match between real and simulated motions. The measured motion track at each point should be regular and periodic about an equilibrium point in a steady-state system such as this one. Any deviation from this motion, such as the erratic behavior seen at point five, is the result of actuation or measurement error. The simulated motion is significantly different to the measured motion at point five. This is likely due to incorrect real motion measurement. Development of the motion measurement system to minimize the motion error should improve the match between the real and simulated data in cases such as this.

Examination of Figure 6 confirmed that 12.5 kPa was most likely the stiffness of the gelatin phantom when actuated at 50 Hz. A 12.5 kPa stiffness gave the lowest motion error when compared to the experimentally measured motion. In addition, assuming the phantom was 12.5 kPa and simulating a noisy motion data set generated an error plot that effectively matched the plot for the experimentally measured data. This result indicates that 12.5 kPa was the likely phantom stiffness, and that 50% experimental noise was a reasonable estimate. This experimental noise came from a variety of sources discussed later in this section.

Investigations using the two other stiffness values with minimum error (6.1 kPa and 9.5 kPa) are shown in Figure 7. Both results showed less similarity to the experimentally measured motion error (overlaid on Figure 7) as the 12.5 kPa data in Figure 6. This confirmed that 12.5 kPa was the most likely apparent stiffness of the phantom when actuated at 50 Hz.

Slight frequency hardening of the gelatine is one reason why the reconstructed stiffness value of 12.5 kPa was higher than the measured static compressive Young's modulus of 9 kPa. In addition, the gelatine was forms a stiffer surface skin when exposed to air. The effect of this stiffer surface skin is readily visible in rows 1–3 of the montage in Figure 4. This stiffer surface skin makes surface motions appear as if they were from a homogeneous phantom of slightly higher stiffness than samples mechanically tested with the outer skin removed.

As with any experimental work, this investigation was subject to sources of experimental error. While these errors were not large enough to significantly compromise the results obtained, documenting the sources of error will allow future work to improve accuracy in all areas.

The measured Young's modulus of the gelatine sample (9 kPa) was slightly below the target range for the experiment (10–50 kPa). This result was

largely due to variability in the phantom preparation process. Though refinements in both phantom preparation and the experimental setup will allow stiffer phantoms to be tested, the motion tracking and stiffness estimation methods used in this experiment will work with phantoms of any stiffness.

The static Young's modulus of 9 kPa may not have been the most accurate description of the elastic properties of the dynamically actuated gelatine, which was observed to have slight viscoelasticity when harmonically actuated. A viscoelastic material has both real (storage modulus) and imaginary (loss modulus) components to the elastic modulus, in this case estimated with a single Young's modulus value. Viscoelastic effects will be considered in future mechanical testing, allowing them to be accounted for in the FE simulation.

Errors were also introduced to the motion data from the detected position of the reference points. The shape and border of each point was not entirely uniform due to diffusion of the permanent marker dye and inaccuracies in its application. Reflections from the surface of the phantom and non-uniformities in lighting meant the appearance of each reference point was not consistent throughout the full range of steady-state motion, reducing the accuracy of reference point localization.

Because the experimental motion data generally followed an ellipsoidal pattern, it was not always easily approximated by a vector. In certain cases (e.g. point five in Figure 5), the reference point motion could not be approximated by an ellipsoid, posing a further challenge. In this case, the estimated motion vector was likely to be incorrect in direction, amplitude, or both.

The motion tracking and processing system does not currently have the ability to determine phase offset of the experimentally measured motion. Additionally, the current FE model can not simulate viscoelastic behavior, and all simulated motion is considered in phase. As a consequence, experimental motions were assumed in phase. While this approach meant that the actual motion error values may have been slightly incorrect, error calculation results were kept consistent, allowing valid comparisons to be made.

Additional errors have been introduced by the use of ellipsoidal path-lines generated by the reference points during the motion cycle to generate vector displacements at nodal points on the phantom model. Such path-lines represent the trace of a particle moving through a motion field, rather than the exact amplitude of the motion field at a (nodal) point in space. A better approximation would be to use the points along the path-lines to determine the local motion field values in the model region immediately surrounding the ellipsoid through a least squares process.

The linear finite element model used in this experiment did not take into account possible geometric and material non-linearity in the gelatine phantom. There is evidence of this in Figures 6 and 7, where peaks in the motion error occur when the simulated model is actuated at a resonant frequency. It is not anticipated that this will cause problems with motion comparison however, as the actuation frequency of the system is variable, and resonant frequencies can be avoided. In addition, the small displacements observed in the real model (1mm) confirm that using a linear finite element model does not in this case lead to significant inaccuracies due to the small displacement assumption.

A comprehensive consideration of the error range of the reconstructed stiffness estimate was not done at this experimental proof of concept stage. Such an investigation would involve repeated tests to build up a pool of data that could be analyzed for variance. This more detailed system characterization will be one of the targets of future research.

Improving motion capture techniques will allow more accurate phantom motion measurement. More consistent motion patterns that can be accurately converted to a FE field representation in turn increases the accuracy of modulus estimation. Future goals include applying reconstruction algorithms to phantoms of a non-homogeneous nature that more closely represent the human breast, which is the ultimate target of the DIET system.

5 Conclusion

The aim of this experiment was to investigate surface motion capture and basic stiffness reconstruction of soft tissue emulating gelatine phantoms. Reference points on the surface of a cylindrical phantom of the same size order as a human breast were tracked across two complete steady-state motion cycles. Mechanical property testing of the gelatine material determined an approximate Young's modulus, which was successfully estimated independently using a FE model and a least squares error fitting approach. Future work will concentrate on creating more accurate phantom motion data sets. These will be used as input to a more sophisticated inversion algorithm with the ability to resolve differences in stiffness between phantoms and within a single phantom.

References

[1] T.A. Krouskop, T.M. Wheeler, F. Kallel, B.S. Garra, and T. Hall. Elastic moduli of breast and prostate tissues under compression. *Ultrasonic Imaging*, 20:260–274, 1998.

[2] A. Samani, J. Bishop, C. Luginbuhl, and D.B. Plewes. Measuring the elastic modulus of ex vivo small tissue samples. *Phys. Med. Biol.*, 48:2183–2198, 2003.

[3] E.E.W. Van Houten, M.M. Doyley, F.E. Kennedy, J.B. Weaver, and K.D. Paulsen. Initial in vivo experience with steady-state subzone-based MR elastography of the human breast. *Journal of Magnetic Resonance Imaging*, 17:72–85, 2003.

[4] F. Kallel and M. Bertrand. Tissue elasticity reconstruction using linear perturbation method. *IEEE Trans. on Medical Imaging*, 15:299–313, 1996.

[5] K. Hoyt, F. Forsberg, C.R.B. Merrit, J-B. Liu, and J. Ophir. In vivo elastographic investigation of ethanol-induced hepatic lesions. *Ultrasound in Medicine and Biology*, 31:607–612, 2005.

[6] S.K. Moore. Better breast cancer detection. *IEEE Spectrum*, 38:50–54, 2001.

[7] L. Gao, K.J. Parker, R.M. Lerner, and S.F. Levinson. Imaging the elastic properties of tissue - a review. *Ultrasound in Medicine and Biology*, 22:959–977, 1996.

[8] M.M. Doyley, J.B. Weaver, E.E.W. Van Houten, F.E. Kennedy, and K.D. Paulsen. Thresholds for detecting and characterizing focal lesions using steady-state MR elastography. *Medical Physics*, 30:495–504, 2003.

[9] J. Bercoff, S. Chaffai, M. Tanter, L. Sandrin, S. Catheline, M. Fink, J.L. Gennisson, and M. Meunier. In vivo breast cancer detection using transient elastography. *Ultrasound in Medicine and Biology*, 29:1387–1396, 2003.

[10] A. Peters, A. Milsant, J. Rouzé, L. Ray, J.G. Chase, and E.E.W. Van Houten. Digital Image-based Elasto-Tomography: Proof of concept

studies for surface-based mechanical property reconstruction. *JSME International Journal*, 47:1117–1123, 2004.

[11] T.J. Hall, M. Bilgen, M.F. Insana, and T.A. Krouskop. Phantom materials for elastography. *IEEE Transactions on Ultrasonics, Ferroelectrics, and Frequency Control*, 44:1355–1365, 1997.

Ingredient	Amount	Weight %
Gelatine	20 g	5.8
2-Propanol	25 ml	5.6
Distilled Water	300 ml	87
Formaldehyde	3 ml	0.97
Total		100

Table 1: Composition of the gelatine phantom used in the experiment.

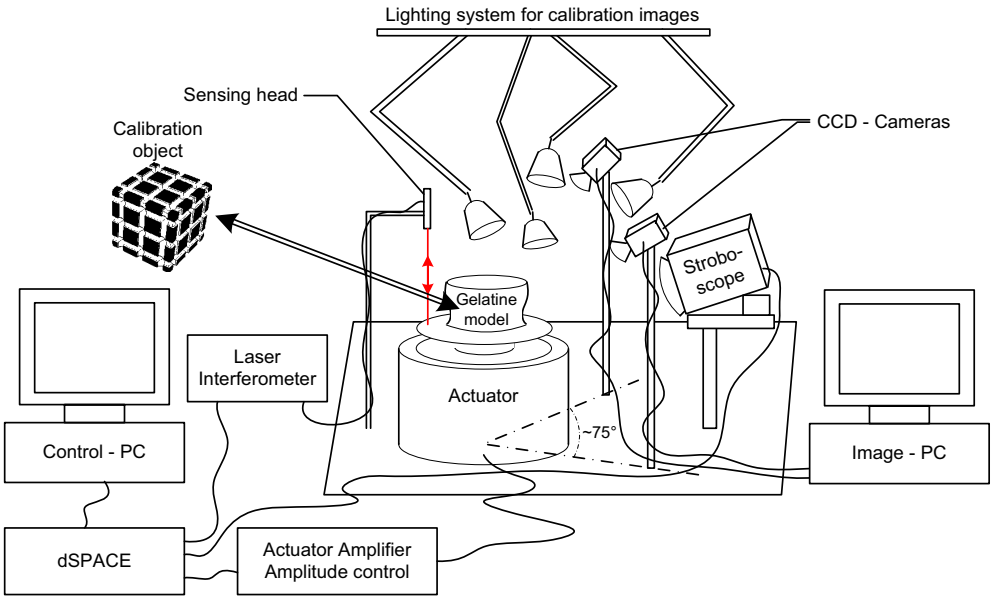

Figure 1: Diagram of experimental setup for phantom actuation and motion capture.

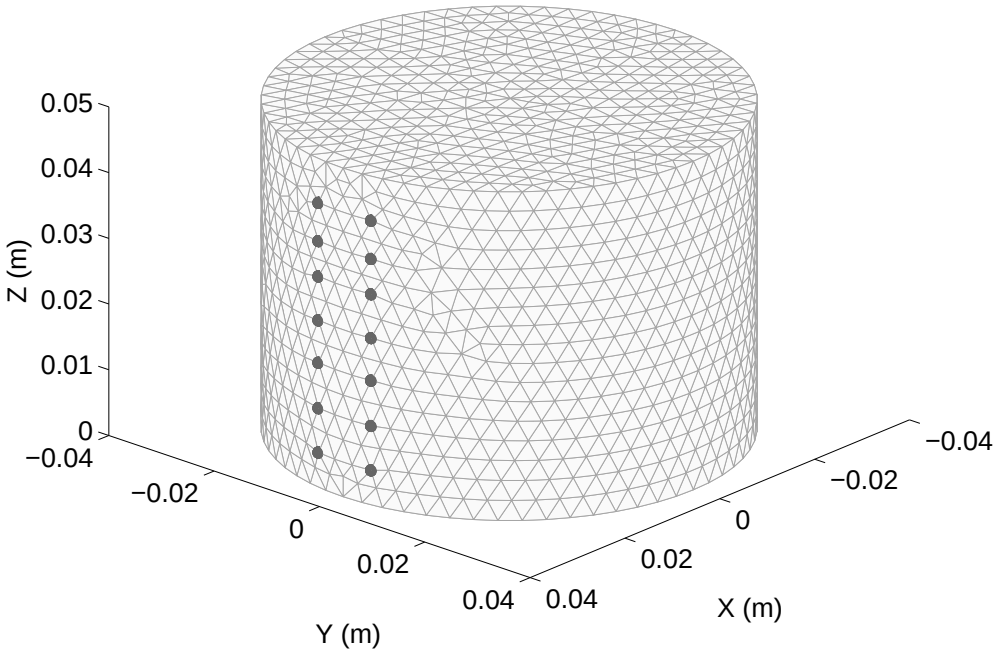

Figure 2: Finite element model used to simulate phantom displacement at a range of stiffness values. The fourteen reference locations that correspond to measured motion points are shown in two columns. The left column includes point 1 (top) through point 7 (bottom), with the right column containing points 8 (top) through 14 (bottom).

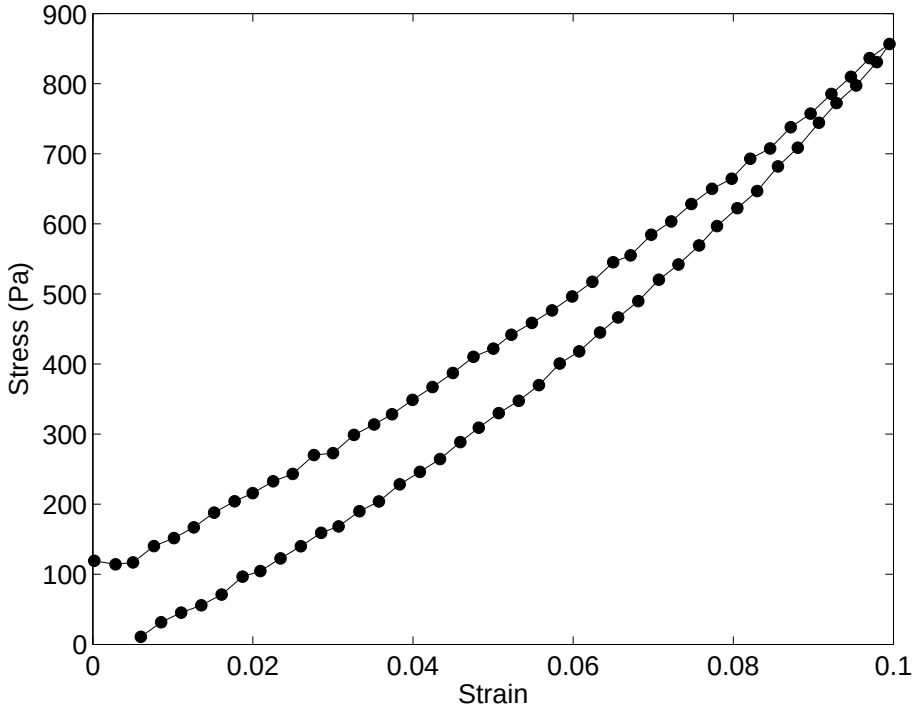

Figure 3: Stress-strain plot for the statically tested gelatine sample. Compressive loading occurred along the upper line while unloading follows the lower line. The slight hysteresis observed is typical of a of viscoelastic material. The small initial pre-load was introduced applied during sample mounting; however, this does not significantly affect the resulting stiffness estimate at these very low strains.

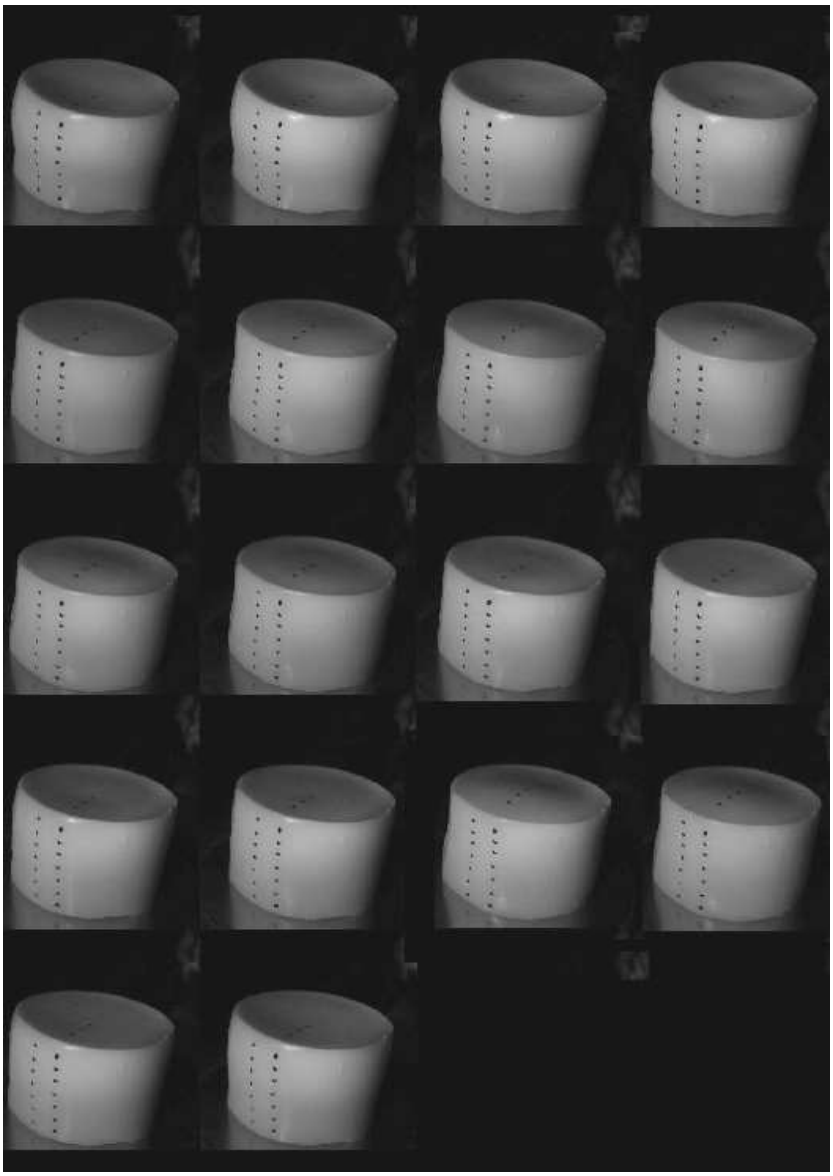

Figure 4: Motion data captured from the left camera across one motion cycle. Images are arranged row-wise, with a phase offset between images of twenty degrees.

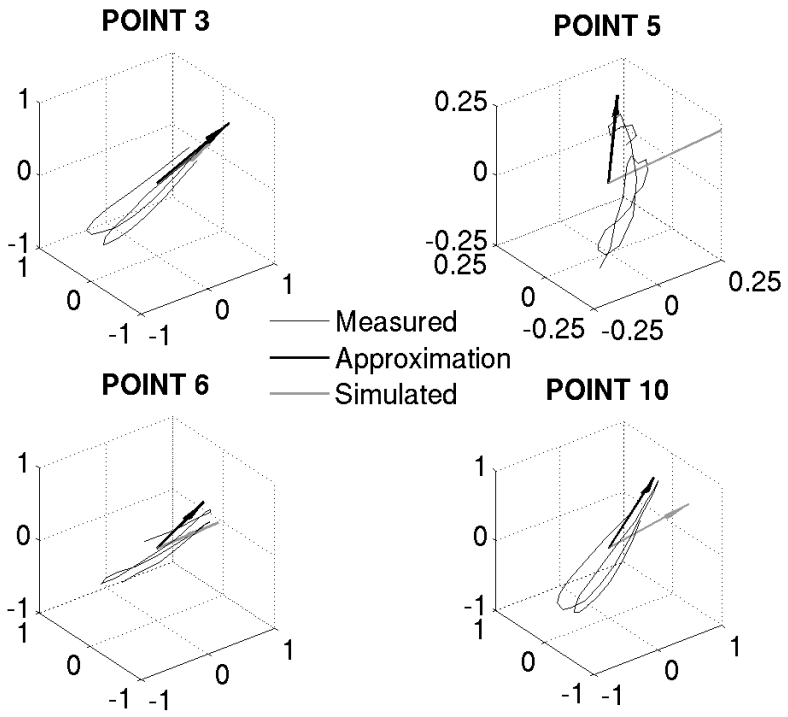

Figure 5: Measured reference point motions with vector approximations for selected reference points on the phantom surface. Points three, six and ten show clear steady-state motion, while the erratic motion at point five made it harder to approximate. The second, light grey, vector on each plot is the FE-simulated motion at a phantom stiffness of 12.5 kPa. This simulated vector at point five has an amplitude of 1.43 mm and has been truncated at the edge of the axis shown to highlight details of the measured motion trace. All axis scales are in mm.

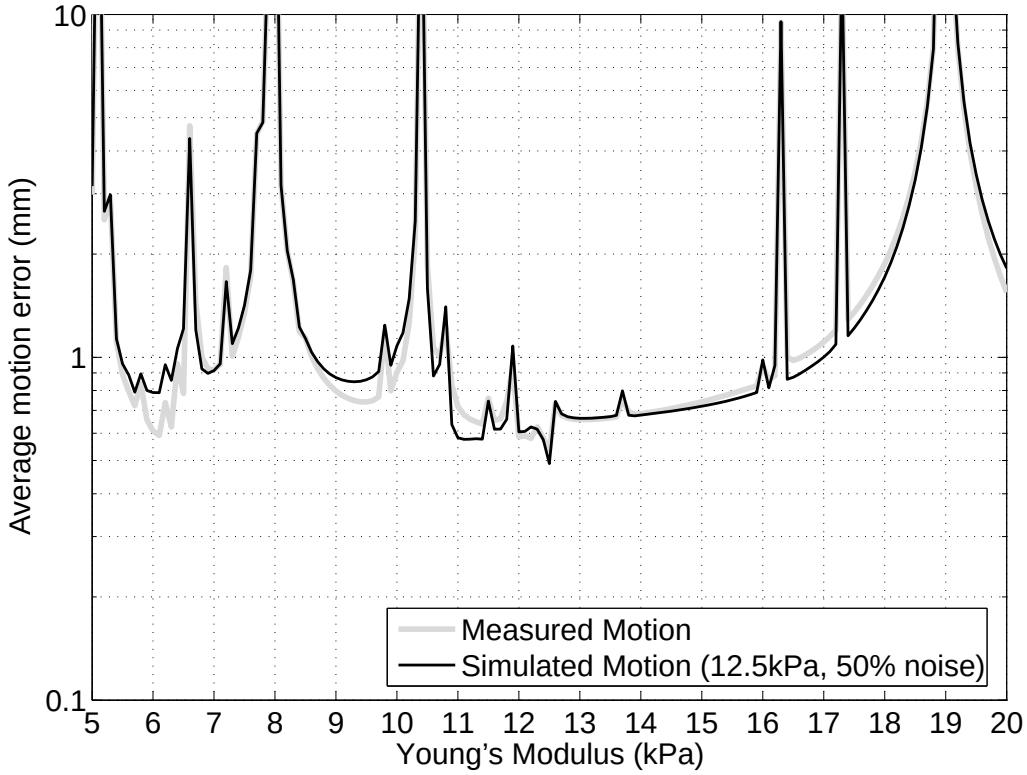

Figure 6: A plot of motion error across a range of stiffness values. The measured motion line represents error between the experimentally measured motion and FE-simulated motion sets at the given Young's modulus value. The simulated motion line represents the same calculations performed assuming that the phantom was 12.5 kPa with the addition of 50% normally distributed noise.

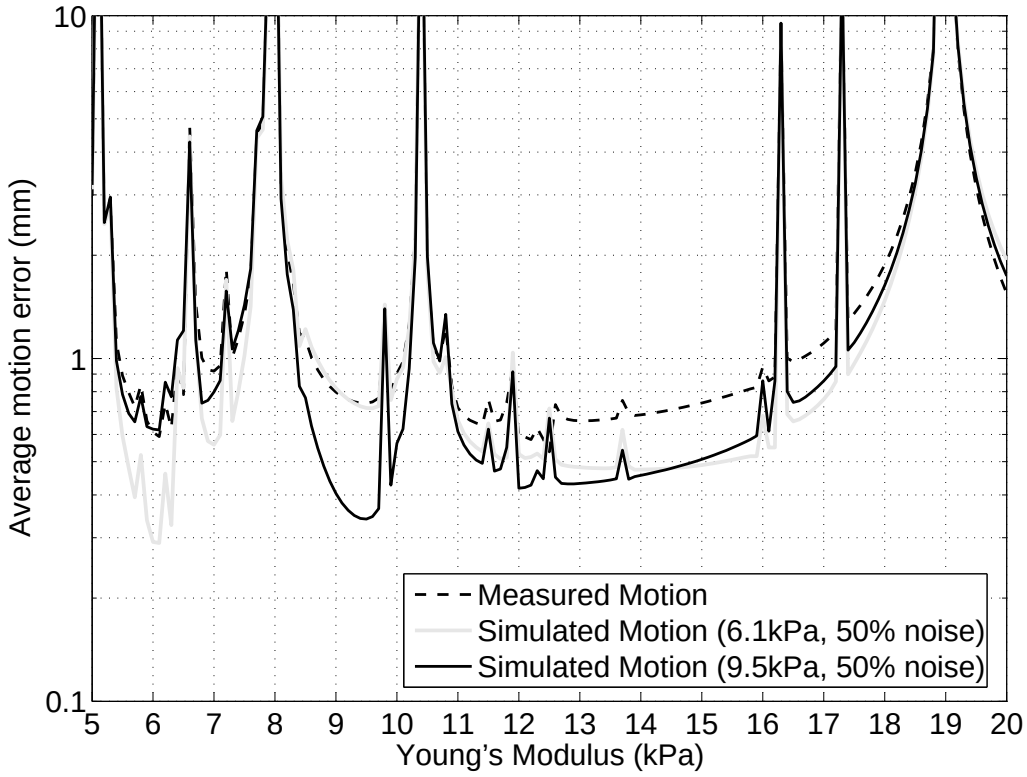

Figure 7: Similar to Figure 6. Here the two simulated results correspond to surface motions from FE models with 6.1 kPa and 9.5 kPa moduli after 50% noise has been added. In general, agreement between simulated and experimental results is not as good as the correspondence between the 12.5 kPa FE simulation and the experimental measurements.